Nanoscale

COMMUNICATION

View Article Online
View Journal | View Issue

Aligned carbon nanotube array stiffness from stochastic three-dimensional morphology†

Itai Y. Stein,[a] Diana J. Lewis[b] and Brian L. Wardle*[b]

Cite this: *Nanoscale*, 2015, **7**, 19426

Received 18th September 2015,
Accepted 28th October 2015

DOI: 10.1039/c5nr06436h

www.rsc.org/nanoscale

The landmark theoretical properties of low dimensional materials have driven more than a decade of research on carbon nanotubes (CNTs) and related nanostructures. While studies on isolated CNTs report behavior that aligns closely with theoretical predictions, studies on cm-scale aligned CNT arrays (>10^{10} CNTs) oftentimes report properties that are orders of magnitude below those predicted by theory. Using simulated arrays comprised of up to 10^5 CNTs with realistic stochastic morphologies, we show that the CNT waviness, quantified *via* the waviness ratio (w), is responsible for more than three orders of magnitude reduction in the effective CNT stiffness. Also, by including information on the volume fraction scaling of the CNT waviness, the simulation shows that the observed non-linear enhancement of the array stiffness as a function of the CNT close packing originates from the shear and torsion deformation mechanisms that are governed by the low shear modulus (~1 GPa) of the CNTs.

Fully utilizing the intrinsic mechanical properties of nanowires, nanofibers, and nanotubes in high value applications has motivated research into control of process and morphology factors that govern their performance in scaled architectures. Many previous studies focused on one particular one-dimensional system, carbon nanotubes (CNTs), due to their highly scalable synthesis techniques, which enable wafer-scale manufacturing and CNT lengths approaching the meter-scale,[1] and an intrinsic elastic modulus ≳1 TPa.[1,2] But such a figure for the elastic modulus of the CNTs could only be attained for architectures comprised of a few isolated pristine and straight CNTs,[2–5] where the idealizations used in early theoretical work are reasonable. However, in large assemblies, where the CNTs normally have non-ideal morphologies, elastic moduli that are up to three orders of magnitude lower than expected were observed.[6–12] See Fig. 1 for a plot of the reported CNT elastic modulus scaled by the CNT volume fraction (V_f) as a function of the number CNTs that comprise the architecture. This large discrepancy in the mechanical behavior of CNTs in scalable structures, such as CNT arrays, originates from their compli-

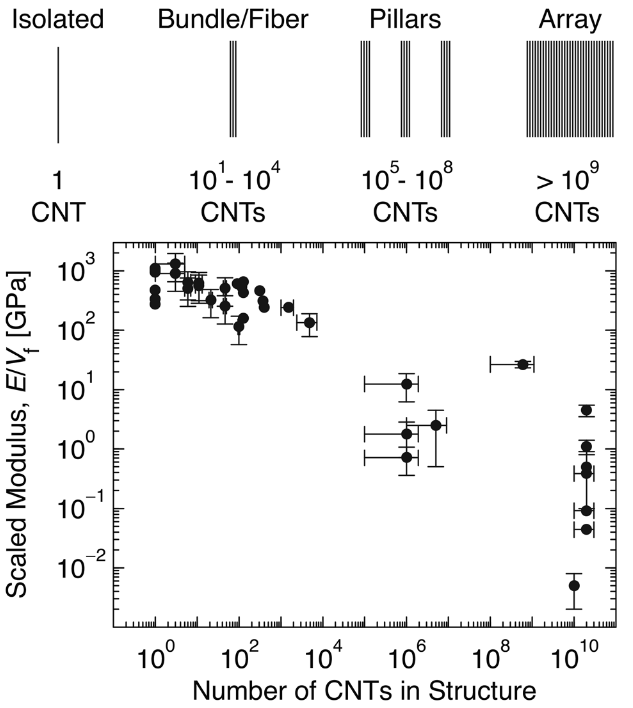

Fig. 1 Reported stiffness for CNT systems as a function of their size. The plot shows how the elastic modulus (E), when normalized by the CNT volume fraction (V_f), scales with the number of CNTs enclosed in the structure demonstrating that isolated CNTs and CNT bundles/fibers exhibit E/V_f > 100 GPa,[2–7] whereas larger scale CNT pillars and arrays exhibit $E/V_f \lesssim 1$ GPa.[8–12]

---

[a] *Department of Mechanical Engineering, Massachusetts Institute of Technology, 77 Massachusetts Ave, Cambridge, MA 02139, USA*

[b] *Department of Aeronautics and Astronautics, Massachusetts Institute of Technology, 77 Massachusetts Ave, Cambridge, MA 02139, USA. E-mail: wardle@mit.edu*

† Electronic supplementary information (ESI) available: Additional simulation details (eqn (S1), (S2) and Fig. S1, S2); mean and standard deviation of the experimentally evaluated waviness ratio and evaluated sinusoidal and helical tortuosity (eqn (S3), Fig. S3, and Table S1), additional mechanical behavior modeling details (eqn (S4), (S5) and Fig. S4), and guide for using this simulation framework for studying the 3D morphology and elastic properties of nanofiber arrays. See DOI: 10.1039/C5NR06436H

cated morphology and the local curvature, commonly known as waviness, that results from their synthesis process.[13,14] Here we report a simulation framework that is capable of re-creating the stochastic morphology of CNTs in three dimensions, and use arrays comprised of >10^5 simulated wavy CNTs to show how waviness leads to the observed orders of magnitude reduction in the stiffness of the CNT arrays.

Previous work on the mechanical behavior of CNTs and their architectures has shown that deviations from the normally assumed straight cylindrical column structure of the CNTs can lead to large reductions in their effective elastic modulus.[15–17] These reductions in stiffness could originate from the large anisotropy in the elastic modulus of the CNT, where the longitudinal modulus can exceed 1 TPa,[2–5,18] a value similar to the in plane modulus of graphene,[19] but the radial shear modulus can be as low as 0.1 GPa,[18] a value similar to the transverse shear modulus of turbostratically stacked graphene/graphite.[20,21] However, while recent work has shown that waviness is the primary morphological effect responsible for the large reduction in the stiffness of CNTs in CNT arrays,[22] these results were obtained using a highly idealized sinusoidal CNT geometry and assumed deformation mechanisms, meaning that the physics underlying the CNT mechanical behavior were not explored in detail. The deformation mechanisms that contribute to the elastic response of wavy CNTs were previously explored in detail for a similar one-dimensional carbon system, the carbon nanocoil, and showed that there are significant contributions by the torsion and shear mechanisms that are normally neglected.[23,24] However, while these results are applicable to the simple helix geometry that carbon nanocoils exhibit, wavy CNTs exhibit a more complicated three-dimensional morphology that cannot be adequately described using simple geometrical models. Here we use three-dimensional descriptions of the morphology of observed arrays of CNTs to study the contribution of (axial) stretching, shear, bending, and torsion on the deformation wavy CNTs, and show that the observed large reductions in stiffness of CNT arrays originate from the deformation mechanisms (torsion and shear) dominated by the low shear modulus of the CNTs.

To simulate the morphology of CNTs in three dimensions, each CNT was discretized into an array of nodes in *xyz* space. The width of the confining two dimensional area that bounds the node displacements was defined using the minimum and maximum inter-CNT spacings (*e.g.* ≈64 nm and ≈92 nm at $V_f \approx 1$ vol.% CNTs) quantified previously,[25,26] and include the evolution of the packing morphology of the CNTs as their volume fraction is increased *via* densification. To apply the appropriate waviness to all nodes, the displacement of each node relative to the node that precedes it was evaluated using the amplitude (a) extracted from the waviness ratio (w) previously quantified experimentally assuming a sinusoidal functional form. a was evaluated using $a = w \times \lambda$, where λ is the characteristic wavelength that has a value equal to the maximum inter-CNT spacing,[25,26] and physically represents the formation of a carbon nanocoil-like morphology at $w \gtrsim 0.5$. To replicate the randomness of the CNT waviness, Gaussian distributions were used to independently evaluate the x and y displacements of the nodes. This method for treating waviness ensures that the CNT waviness is stochastic, leading to simulated CNTs with more realistic and truly three-dimensional morphologies. Also, while this method does not explicitly include CNT–CNT interactions in the CNT morphology evolution, such as the van der Waals (vdW) interactions used in recent modeling efforts,[27–29] the resulting randomness of the CNT array morphology implicitly accounts for fluctuations in their electrostatic interactions, while avoiding the assumption of the idealized vdW potential that may not accurately describe the behavior of CNTs with native defects and other adsorbed species.[26] The main difference between the current method, and modeling efforts that include vdW interactions, is that CNT arrays simulated here might have fewer CNT–CNT junctions, *i.e.* a more uniform local V_f, but such an effect will be very small when averaged over a sample size of 10^5 CNTs. $n \times n$ large CNT arrays were then assembled layer-by-layer, where each layer was comprised of n wavy CNTs enclosed in their confining area, and the layers were arranged in a manner analogous to Bernal stacking (*i.e.* ABAB type stacking) to ensure that the representative packing morphology, defined by the effective two-dimensional coordination number,[25] is satisfied. See Fig. 2a for a top view illustrating the two-dimensional random walk of a wavy CNT in a square confining area, and the resulting simulated wavy CNT array. Since the local radius of curvature (R_c) of the CNTs strongly influences their mechanical behavior, the node displacements that comprise the two dimensional random walk, along with the node separation in the $\hat{z}$ direction, were used to evaluate R_c (see eqn (S1) in section S1 of the ESI†). See Fig. 2b for an illustration of R_c evaluated using 10 nodes, and the scaling of R_c with w and V_f. As Fig. 2b demonstrates, R_c plateaus at $0.1 \leq w \leq 0.3$ and has a value of ~1 nm for $V_f = 40\%$ CNTs, a value that is on the same order of the curvature of ripples that are expected to form on the surface of ~8 nm diameter (~1.5 nm wall thickness) CNT during buckling,[30,31] indicating that the simulation results are physical for $V_f \leq 40\%$ CNTs. A note should be made that $R_c \sim 1$ nm is on the same order as the variations in the CNT inner and outer diameter that were reported previously,[32] and that such nanoscale surface features can arise through either Stone-Wales or inter-wall defects.[33–36] To ensure that R_c is evaluated for an amount of waviness that is generalizable to other non-stochastic descriptions, *e.g.* sinusoidal or helical functional forms, the node separation in the $\hat{z}$ direction was controlled so that the ratio of the true length of the CNTs (L_{cnt}) to the measured height of the CNT array in the $\hat{z}$ direction (H), also known as the tortuosity (τ), for the stochastic system matched the L_{cnt}/H ratio (*i.e.* τ) for the deterministic sinusoidal description at each value of w. See section S2 in the ESI† for details. To evaluate the impact of CNT proximity effects on their morphology, the evolution of w as a function of the V_f was quantified.

The waviness of the aligned CNT arrays was evaluated using a simple sinusoidal amplitude-wavelength (a/λ) definition of

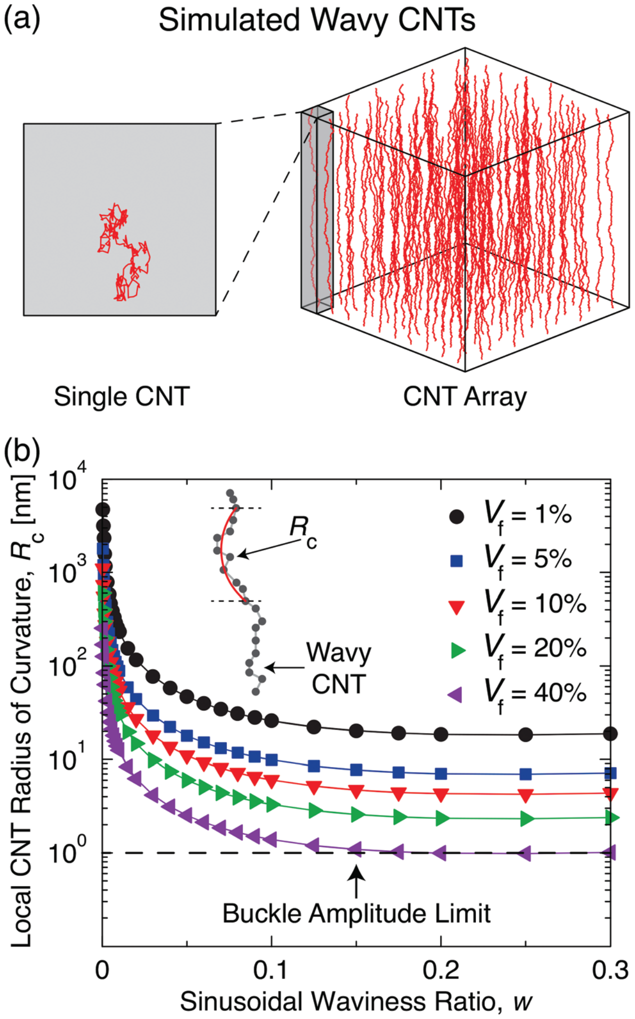

Fig. 2 Simulation framework and CNT waviness integration. (a) Top view of a simulated CNT illustrating the two dimensional random walk that comprises the waviness inside of the confining area, and side view of an aligned array of simulated wavy CNTs. (b) Plot showing the evolution of the CNT alignment, represented by the local radius of curvature (R_c), as a function of the waviness ratio (w).

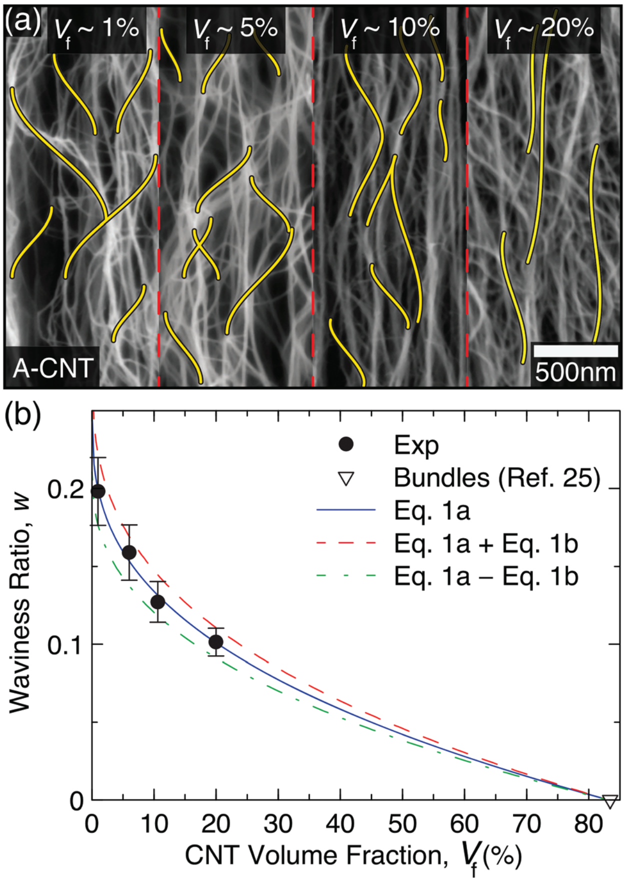

Fig. 3 Evolution of the CNT waviness with packing. (a) Cross-sectional scanning electron microscopy (SEM) micrographs of CNT arrays at volume fractions (V_f) ranging from ~1–20 vol.% CNTs showing the reduction in CNT waviness. (b) Plot demonstrating that the waviness ratio (w) can be reduced by ~50% by increasing V_f from ~1 vol.% CNTs to ~20 vol.% CNTs.

the waviness ratio (w), and was approximated from scanning electron microscope (SEM) images of the cross-sectional morphology of the CNT arrays. See Fig. 3a for exemplary SEM micrographs of CNT arrays as a function of V_f taken using a high resolution SEM (JEOL 6700, 3.0 mm working distance, 1–1.5 kV accelerating voltage),[25,26,32] and for an illustration of the waviness quantification using a sinusoidal definition of w. Since SEM images of the morphology of the CNT arrays are projections of a three-dimensional system onto a two-dimensional surface, information about the waviness in the through-thickness direction (*i.e.* the direction parallel to incident electron beam) is lost and must be accounted for. To account for the loss of depth information, a correction factor of $\sqrt{2}$ was applied to simulate a mean view angle of 45° (λ is independent of the view angle and requires no correction). See Fig. 3b for a plot of the evaluated w as a function of V_f. As Fig. 3b illustrates, CNT confinement at higher packing fractions reduces the mean values and statistical uncertainties of w significantly from ~0.2 ± 0.02 at $V_f \approx 1\%$ CNTs to ~0.1 ± 0.01 at $V_f \approx 20\%$ CNTs (see section S2 in the ESI† for details). The values for w at $V_f \sim 1\%$ CNTs are on the same order as ones previously reported for similar CNT systems, $w \simeq 0.2 \pm 0.1$,[37,38] and are in agreement with the recently reported tortuosity ($\rightarrow L_{cnt}/H$) evolution of CNTs during densification, where $\rightarrow L_{cnt}/H$ decreased from ~1.2 ($\rightarrow w \sim 0.15$) at the as-grown state ($V_f \sim 3\%$ CNTs) to ~1.06 ($\rightarrow w \sim 0.08$) for CNTs densified by a factor of 6 × ($V_f \sim 20\%$ CNTs).[32] Since the statistical uncertainty (and standard deviation) of w decreases significantly during packing, but the CNT morphology remains very stochastic (the standard deviation of w is consistently at $\gtrsim 50\%$ of the mean value of w as shown by Table S1 in the ESI†), representative descriptions of the CNT waviness and morphology must account for both the mean and uncertainty in w. Therefore, to simulate the observed scaling of waviness as a function of V_f, both the mean (μ_w) values of w and the statistical uncertainties in $\mu_w(\sigma_w/\sqrt{n})$ were fit independently *via* power laws using the theoretical maximum V_f of 83.45% CNTs, where both the mean and standard deviation of w have a value of 0,[25] leading to the following scaling relations:

$$\mu_w(V_f) = a_1(V_f)^{b_1} + c_1 \tag{1a}$$

$$\sigma_w(V_f)/\sqrt{n} = a_2(V_f)^{b_2} + c_2 \tag{1b}$$

where $a_1 = -0.04967$, $b_1 = 0.3646$, and $c_1 = 0.2489$ with coefficient of determination ($\mathbb{R}^2$) of 0.9996, and $a_2 = 0.0852/\sqrt{n}$, $b_2 = 0.2037$, $c_2 = 0.2100/\sqrt{n}$, and $n = 30$ CNTs with $\mathbb{R}^2 = 0.9812$. Using the scaling relations presented in eqn (1), the impact of waviness on the mechanical behavior of CNT arrays was explored.

The stiffness of a wavy CNT is analyzed using the principle of virtual work, similar to a previous study of the deformation of a carbon nanocoil.[23] In this analysis, four deformation mechanisms are considered: extension, shear, bending, and torsion. See Fig. 4a for an illustration of the four modes that contribute to the deformation of a wavy CNT, and the scaling of their compliance contribution as a function of w. Similar to the previous analysis,[23] one unit cell, which is defined as a segment bound by two nodes in the $\hat{z}$ direction, is used to evaluate the contribution of the four deformation modes. However, unlike the previously explored helical carbon nanocoils,[23] the wavy CNTs simulated here arestochastic, *i.e.* a random walk in three dimensions, such that the geometry of the unit cell in the x–y plane needs to be determined numerically for each node of a wavy CNT instead of being defined analytically as would be the case for other deterministic descriptions of waviness, *e.g.* sine waves or helices. See section S1 in the ESI† for all correlations used to define the unit cell. The extension ($\xi_{\text{extension}}$), shear (ξ_{shear}), bending (ξ_{bending}), andtorsion (ξ_{torsion}) contributions to deformation can be expressed as follows:[23]

$$\xi_{\text{extension}} = \left(\frac{\zeta(w)^2}{4\chi(w)^2 + \zeta(w)^2}\right)\left(\frac{L}{YA}\right) \tag{2a}$$

$$\xi_{\text{shear}} = \left(\frac{4\chi(w)^2}{4\chi(w)^2 + \zeta(w)^2}\right)\left(\frac{L\alpha}{GA}\right) \tag{2b}$$

$$\xi_{\text{bending}} = \left(\frac{\chi(w)^2\zeta(w)^2\lambda^2}{4\chi(w)^2 + \zeta(w)^2}\right)\left(\frac{L}{YI}\right) \tag{2c}$$

$$\xi_{\text{torsion}} = \left(\frac{4\chi(w)^4\lambda^2}{4\chi(w)^2 + \zeta(w)^2}\right)\left(\frac{L}{GJ}\right) \tag{2d}$$

where w is the waviness ratio, λ is the wavelength of the waviness, $\chi(w)$ represents the average displacement of the CNTs in the x–y plane from their 2D random walk, $\zeta(w)$ quantifies the separation of the two nodes that bound the unit cell in the $\hat{z}$ direction, L is the arc length of the CNT between the two nodes in the $\hat{z}$ direction ($= \tau\Delta z$), Y and G are the intrinsic elastic ($\rightarrow Y = 1$ TPa)[1,2] and shear ($\rightarrow 0.1$ GPa $\lesssim G \lesssim 2$ GPa) moduli of the CNT walls,[18,39] A is the cross-sectional area of the CNTs (hollow cylinder geometry), I and J are the area and

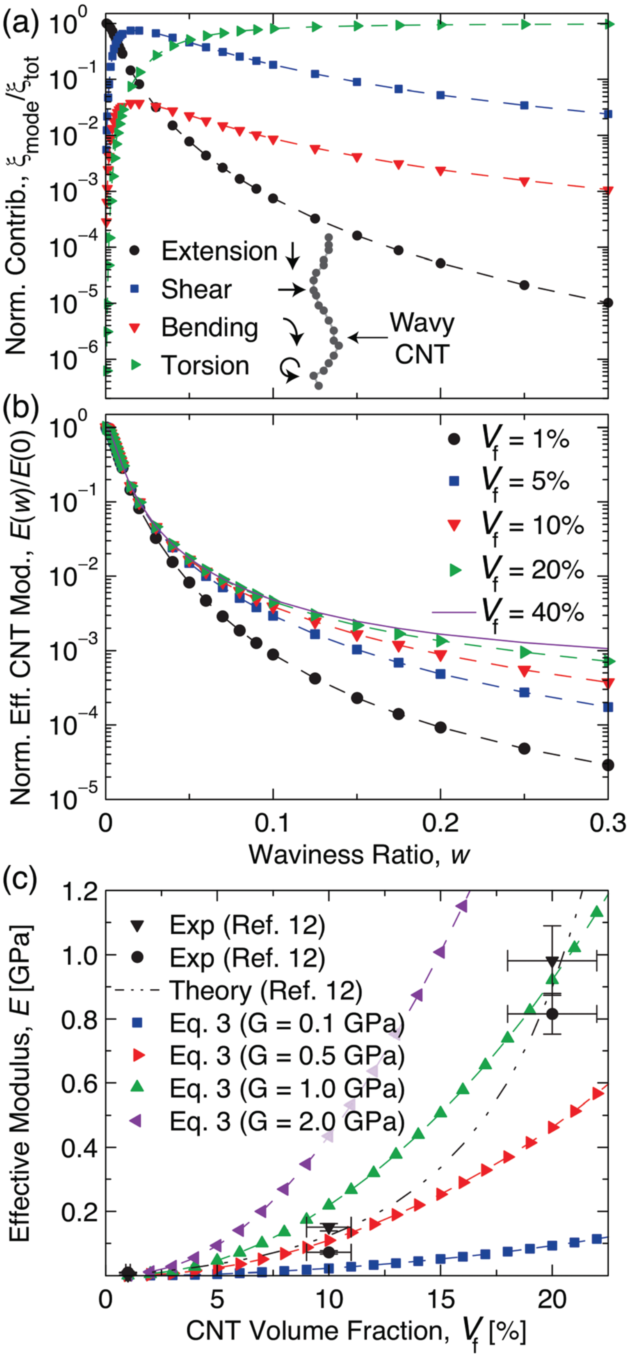

Fig. 4 Elastic response of wavy aligned CNTs. (a) Illustration and scaling of the compliance contribution ($\rightarrow\xi_{\text{mode}}/\xi_{\text{tot}}$ where $\xi_{\text{tot}} = \sum\xi$) of the four deformation modes as a function of the waviness ratio (w) at CNT volume fraction (V_f) of V_f = 1% CNTs. (b) Plot of the effective modulus of wavy CNTs ($E(w)$) normalized by the intrinsic modulus of straight CNTs ($E(0)$) as a function of w and V_f indicating that waviness can lead to orders of magnitude reductions in modulus. (c) Plot comparing the scaling of the effective modulus with V_f ($\rightarrow E(V_f)$) for the 10^5 simulated wavy CNTs (*via* eqn (3)) to the previously reported experimental and theoretical scaling of $E(V_f)$.[12] This plot shows that the shear modulus (G) of the CNTs, which dominates the torsion and shear deformation mechanisms, governs the scaling of $E(V_f)$.

polar (*i.e.* torsion) moments of inertia of a hollow cylinder exhibiting the inner (D_i) and outer (D_o) diameters of the CNTs, and α is the shear coefficient.[18] A, I, and J are evaluated using $D_\mathrm{i} \sim 5$ nm and $D_\mathrm{o} \sim 8$ nm,[32,40] which are representative of the CNTs studied here and in ref. 12. See section S3 in the ESI† for additional information about the mechanical behavior analysis, and section S4 in the ESI† for a detailed guide of how the CNT array mechanical properties were evaluated from their 3D morphology. Using eqn (2) and the volume fraction of the CNTs (V_f), the effective spring constant ($K(w)$) and effective elastic modulus ($E(w)$) of the CNT arrays can be defined as follows:

$$K(w) = (\xi_\mathrm{extension} + \xi_\mathrm{shear} + \xi_\mathrm{bending} + \xi_\mathrm{torsion})^{-1} \tag{3a}$$

$$E(w) = K(w)\left(\frac{L}{A}\right)V_\mathrm{f} \tag{3b}$$

See Fig. 4b for a plot of the ratio of the modulus scaling of wavy CNTs (→$E(w)$) from eqn (3) normalized by the modulus of collimated CNTs (→$E(0)$) for $G \sim 1$ GPa. As Fig. 4b demonstrates, CNT waviness significantly impacts their mechanical properties, and leads to a two orders of magnitude drop in modulus (→$E(w)/E(0) \gtrsim 10^{-2}$) at $w \sim 0.05$ and three orders of magnitude drop in modulus (→$E(w)/E(0) \gtrsim 10^{-3}$) at $w \gtrsim 0.2$ for CNTs with $D_\mathrm{o} \sim 8$ nm. This large change in $E(w)$ is attributed to the small value of G in the CNTs, which is more than three orders of magnitude smaller than Y, and leads the shear (see eqn (2b)) and torsion (see eqn (2d)) deformation modes to contribute ≳98% of the effective compliance of the wavy CNTs at $w \gtrsim 0.05$ (see Fig. S4 in the ESI†). Since the CNTs studied here are treated as non-interacting and cannot escape their confining volumes, the impact of the size of the confining box on the CNT array effective modulus was evaluated by varying V_f from 1% CNTs to 40% CNTs. As Fig. 4b illustrates, the as-grown CNT arrays ($V_\mathrm{f} \approx 1\%$ CNTs), which have waviness characterized by the largest local curvature and experience a larger torsion contribution (≳50% of the effective CNT compliance at $w \gtrsim 0.05$, see Fig. 4a), exhibit the largest reductions in effective modulus due to waviness, *e.g.* $E(w)/E(0) \gtrsim 10^{-4}$ at $w \sim 0.20$, while densified CNTs ($V_\mathrm{f} \gtrapprox 5\%$ CNTs), which have incrementally smaller local curvature (see Fig. 2b) and exhibit a larger shear contribution (≳80% of effective compliance at $w \gtrsim 0.02$, see Fig. S4 in the ESI†), are less sensitive to waviness and see smaller reductions in the CNT effective stiffness with w, *e.g.* $E(w)/E(0)$ for $V_\mathrm{f} \approx 40\%$ CNTs is ≳3× larger than $E(w)/E(0)$ for $V_\mathrm{f} \approx 5\%$ CNTs at $w \gtrsim 0.10$. Using the scaling of w with V_f (→$w(V_\mathrm{f})$ see eqn (1)), eqn (3) can be used to predict the mechanical behavior of CNT arrays as a function of their V_f (→$E(V_\mathrm{f})$). See Fig. 4c for a plot of $E(V_\mathrm{f})$ for 0.1 GPa $\lesssim G \lesssim$ 2 GPa evaluated using 10^5 simulated wavy CNTs (→standard error of ≲0.5%). As Fig. 4c demonstrates, the value of G has a very strong impact on $E(V_\mathrm{f})$, where $G \approx 0.9 \pm 0.3$ GPa agrees very well with the previously reported experimental values of $E(V_\mathrm{f})$ that were approximated using two nanoindentation tip geometries (spherical and Berkovich).[12] In the previous study, the observed large increase in stiffness was explained through a first order theoretical model for collimated (→$w = 0$) CNTs that uses the average inter-CNT separation at a certain V_f (→ranging from 10 nm to 80 nm), and the minimum inter-CNT separation (~5 nm) that is controlled by CNT proximity effects, to approximate $E(V_\mathrm{f})$ given a starting point of $E(V_\mathrm{f} = 1\%) \sim 4$ MPa. While the results of the previously reported theoretical model are in good agreement with the results of the simulated wavy CNTs with $G \approx 0.9 \pm 0.3$ GPa reported here (see Fig. 4c), the simulation results give a clear physical origin for the observed mechanical behavior of the CNT arrays, *i.e.* deformation occurs mostly through shear and torsion, whereas the theoretical model, which had no access to information relating the CNT waviness to their elastic properties,[12] could not provide the morphological origin of the observed behavior. These results illustrate that the inclusion of a representative description of the CNT waviness is necessary to properly describe their mechanical behavior from the underlying physics.

In summary, a simulation framework that enables a representative stochastic description of the magnitude and evolution of the waviness of nanofiber arrays was applied to aligned carbon nanotubes (CNTs) and was used to predict the mechanical behavior of aligned CNT (A-CNT) arrays as a function of the CNT volume fraction. The simulation results indicate that the CNT waviness, quantified *via* the waviness ratio (w), is responsible for more than three orders of magnitude reduction in the intrinsic CNT stiffness. Also, by including information on the volume fraction scaling of both the mean value and statistical uncertainty of the CNT waviness, the simulation is able to replicate the experimentally measured CNT array elastic modulus,[12] and show that the observed non-linear enhancement of the array stiffness as a function of the CNT close packing originates from the low shear modulus of the CNTs which governs the shear and torsion deformation mechanisms. Further work to elucidate the origin of the observed waviness reduction is required, and future study of the morphology of A-CNT arrays in three dimensions *via* a newly developed quantitative electron tomography technique is planned.[41] Also, once additional information on the morphology of A-CNT arrays in three dimensions in available, the CNT–CNT electrostatic interactions in the small (≲10 nm) and intermediate (~10–100 nm) regimes, which may not be purely van der Waals in nature but lead to bundle formation and significant moisture adsorption in ambient conditions,[26] will be analyzed and modeled. Using this simulation framework, more accurate material property predictions for CNT and other nanofiber based architectures may become possible, potentially enabling the design and fabrication of next-generation multifunctional material architectures with integrated sensing and reinforcement capabilities.

Acknowledgements

This work was supported by Airbus, Boeing, Embraer, Lockheed Martin, Saab AB, TohoTenax, and ANSYS through MIT's

Nano-Engineered Composite aerospace STructures (NECST) Consortium and was supported (in part) by the U.S. Army Research Office under contract W911NF-07-D-0004 and W911NF-13-D-0001. I.Y.S. was supported by the Department of Defense (DoD) through the National Defense Science & Engineering Graduate Fellowship (NDSEG) Program. The authors thank John Kane (MIT) and the entire necstlab at MIT for technical support and advice. This work made use of the core facilities at the Institute for Soldier Nanotechnologies at MIT, supported in part by the U.S. Army Research Office under contract W911NF-07-D-0004, and was carried out in part through the use of MIT's Microsystems Technology Laboratories.

References

1 M. F. L. De Volder, S. H. Tawfick, R. H. Baughman and A. J. Hart, *Science*, 2013, **339**, 535–539.

2 B. Peng, M. Locascio, P. Zapol, S. Li, S. L. Mielke, G. C. Schatz and H. D. Espinosa, *Nat. Nanotechnol.*, 2008, **3**, 626–631.

3 M.-F. Yu, O. Lourie, M. J. Dyer, K. Moloni, T. F. Kelly and R. S. Ruoff, *Science*, 2000, **287**, 637–640.

4 M.-F. Yu, B. S. Files, S. Arepalli and R. S. Ruoff, *Phys. Rev. Lett.*, 2000, **84**, 5552–5555.

5 J.-P. Salvetat, G. A. D. Briggs, J.-M. Bonard, R. R. Bacsa, A. J. Kulik, T. Stöckli, N. A. Burnham and L. Forró, *Phys. Rev. Lett.*, 1999, **82**, 944–947.

6 K. Koziol, J. Vilatela, A. Moisala, M. Motta, P. Cunniff, M. Sennett and A. Windle, *Science*, 2007, **318**, 1892–1895.

7 N. Behabtu, C. C. Young, D. E. Tsentalovich, O. Kleinerman, X. Wang, A. W. K. Ma, E. A. Bengio, R. F. ter Waarbeek, J. J. de Jong, R. E. Hoogerwerf, S. B. Fairchild, J. B. Ferguson, B. Maruyama, J. Kono, Y. Talmon, Y. Cohen, M. J. Otto and M. Pasquali, *Science*, 2013, **339**, 182–186.

8 C. P. Deck, J. Flowers, G. S. B. McKee and K. Vecchio, *J. Appl. Phys.*, 2007, **101**, 023512.

9 T. Tong, Y. Zhao, L. Delzeit, A. Kashani, M. Meyyappan and A. Majumdar, *Nano Lett.*, 2008, **8**, 511–515.

10 A. Qiu, D. Bahr, A. Zbib, A. Bellou, S. Mesarovic, D. McClain, W. Hudson, J. Jiao, D. Kiener and M. Cordill, *Carbon*, 2011, **49**, 1430–1438.

11 Y. Won, Y. Gao, M. A. Panzer, S. Dogbe, L. Pan, T. W. Kenny and K. E. Goodson, *Carbon*, 2012, **50**, 347–355.

12 H. Cebeci, I. Y. Stein and B. L. Wardle, *Appl. Phys. Lett.*, 2014, **104**, 023117.

13 S. Pathak, J. R. Raney and C. Daraio, *Carbon*, 2013, **63**, 303–316.

14 M. Bedewy and A. J. Hart, *Nanoscale*, 2013, **5**, 2928–2937.

15 F. T. Fisher, R. D. Bradshaw and L. C. Brinson, *Appl. Phys. Lett.*, 2002, **80**, 4647–4649.

16 F. Fisher, R. Bradshaw and L. Brinson, *Compos. Sci. Technol.*, 2003, **63**, 1689–1703.

17 D. Handlin, I. Y. Stein, R. Guzman de Villoria, H. Cebeci, E. M. Parsons, S. Socrate, S. Scotti and B. L. Wardle, *J. Appl. Phys.*, 2013, **114**, 224310.

18 X.-L. Wei, Y. Liu, Q. Chen, M.-S. Wang and L.-M. Peng, *Adv. Funct. Mater.*, 2008, **18**, 1555–1562.

19 C. Lee, X. Wei, J. W. Kysar and J. Hone, *Science*, 2008, **321**, 385–388.

20 G. Savini, Y. Dappe, S. Öberg, J.-C. Charlier, M. Katsnelson and A. Fasolino, *Carbon*, 2011, **49**, 62–69.

21 X. Chen, C. Yi and C. Ke, *Appl. Phys. Lett.*, 2015, **106**, 101907.

22 N. J. Ginga, W. Chen and S. K. Sitaraman, *Carbon*, 2014, **66**, 57–66.

23 X. Chen, S. Zhang, D. A. Dikin, W. Ding, R. S. Ruoff, L. Pan and Y. Nakayama, *Nano Lett.*, 2003, **3**, 1299–1304.

24 J. Wang, T. Kemper, T. Liang and S. B. Sinnott, *Carbon*, 2012, **50**, 968–976.

25 I. Y. Stein and B. L. Wardle, *Phys. Chem. Chem. Phys.*, 2013, **15**, 4033–4040.

26 I. Y. Stein, N. Lachman, M. E. Devoe and B. L. Wardle, *ACS Nano*, 2014, **8**, 4591–4599.

27 S. Cranford, H. Yao, C. Ortiz and M. J. Buehler, *J. Mech. Phys. Solids*, 2010, **58**, 409–427.

28 Y. Won, Y. Gao, M. A. Panzer, R. Xiang, S. Maruyama, T. W. Kenny, W. Cai and K. E. Goodson, *Proc. Natl. Acad. Sci. U. S. A.*, 2013, **110**, 20426–20430.

29 M. R. Maschmann, *Carbon*, 2015, **86**, 26–37.

30 A. Pantano, D. M. Parks and M. C. Boyce, *J. Mech. Phys. Solids*, 2004, **52**, 789–821.

31 I. Nikiforov, D.-B. Zhang, R. D. James and T. Dumitrică, *Appl. Phys. Lett.*, 2010, **96**, 123107.

32 J. Lee, I. Y. Stein, M. E. Devoe, D. J. Lewis, N. Lachman, S. S. Kessler, S. T. Buschhorn and B. L. Wardle, *Appl. Phys. Lett.*, 2015, **106**, 053110.

33 A. V. Krasheninnikov and K. Nordlund, *J. Appl. Phys.*, 2010, **107**, 071301.

34 Y. Kinoshita, M. Kawachi, T. Matsuura and N. Ohno, *Phys. E (Amsterdam, Neth.)*, 2013, **54**, 308–312.

35 C. D. Latham, M. I. Heggie, M. Alatalo, S. Öberg and P. R. Briddon, *J. Phys.: Condens. Matter*, 2013, **25**, 135403.

36 T. Trevethan, P. Dyulgerova, C. D. Latham, M. I. Heggie, C. R. Seabourne, A. J. Scott, P. R. Briddon and M. J. Rayson, *Phys. Rev. Lett.*, 2013, **111**, 095501.

37 H. Cebeci, R. Guzmán de Villoria, A. J. Hart and B. L. Wardle, *Compos. Sci. Technol.*, 2009, **69**, 2649–2656.

38 U. Vainio, T. I. W. Schnoor, S. Koyiloth Vayalil, K. Schulte, M. Müller and E. T. Lilleodden, *J. Phys. Chem. C*, 2014, **118**, 9507–9513.

39 G. Guhados, W. Wan, X. Sun and J. L. Hutter, *J. Appl. Phys.*, 2007, **101**, 033514.

40 I. Y. Stein and B. L. Wardle, *Carbon*, 2014, **68**, 807–813.

41 B. Natarajan, N. Lachman, T. Lam, D. Jacobs, C. Long, M. Zhao, B. L. Wardle, R. Sharma and J. A. Liddle, *ACS Nano*, 2015, **9**, 6050–6058.